Spinous TiO$_2$ and Au@TiO$_2$ octahedral nanocages: Amorphisity-to-crystallinity transition-driven surface structural construction and photocatalytic study

Jie Li [a], Lianhai Zu [a], Ying Li [a], Chao Jin [a], Yao Qin [b,*], Donglu Shi [b,c], Jinhu Yang [a,b,*]

[a] Department of Chemistry, Tongji University, Siping Road 1239, Shanghai 200092, People's Republic of China
[b] Research Center for Translational Medicine & Key Laboratory of Arrhythmias of the Ministry of Education of China, East Hospital,
Tongji University School of Medicine, No. 150 Jimo Road, Shanghai 200120, People's Republic of China
[c] Materials Science and Engineering Program, Department of Mechanical and Materials Engineering, University of Cincinnati, Cincinnati, OH 45221-0072, United States

ARTICLE INFO

ABSTRACT

Novel spinous TiO$_2$ and Au@TiO$_2$ octahedral nanocages have been prepared through a well-designed three-step strategy including templated TiO$_2$ wet coating, subsequent structural ripening and final template removal or transformation. The strategy is built on an amorphisity-to-crystallinity transition-driven surface structural construction, which emphasizes the critical steps of crystallization-controlled TiO$_2$ coating and consequent structural ripening. The influence of some key parameters, such as coating temperature, ripening temperature and ripening time, on the structure and morphology of the spinous TiO$_2$ and Au@TiO$_2$ nanocages have been investigated. In addition, in photocatalytic measurements, the prepared spinous TiO$_2$-based nanocages exhibit enhanced photocatalytic efficiency relative to spinousless TiO$_2$-based nanocages as well as P-25, owing to their structure advantages resulting from spinous surfaces. The photocatalytic activity of these TiO$_2$ based photocatalysts has been systematically studied through the corresponding ·OH radical measurements. The synthetic strategy may work as a general method, through similarly designing, to realize surface structure engineering for various materials such as metals, hydroxide and other oxides besides TiO$_2$.

© 2014 Elsevier Inc. All rights reserved.

1. Introduction

Interface/surface engineering of nanomaterials is of great significance for both fundamental science and technology [1–5]. TiO$_2$ is a promising semiconductor material with unique properties and important broad applications such as photoelectric area of photocatalysis and photovoltaic devices [6–11]. It is generally admitted that photoelectric processes, in principle, involve the key steps of photoinduced electron-hole pair generation, separation and consequent catalytic oxidation/reduction half reactions initiated by holes/electrons respectively, which are all proceeded at interface/surface of the TiO$_2$ materials [12,13]. As a typical class, hollow structured TiO$_2$ with spherical or non-spherical shapes has received special attention, due to their large interface/surface, high light harvesting, large interior space as well as low density and

high movability that are beneficial for high-performance photoelectric utilizations [3,4,14–19]. For the purpose of obtaining higher performance, considerable progress on specific structural modulation at external/internal interfaces of TiO$_2$ hollow particles has been made. For example, TiO$_2$ hollow spheres with shells consisting of nanosheets had been prepared by alkaline hydrothermal etching or hydrophilic functional group directing method, manifesting enhanced photocatlytic activity [4] and excellent lithium storage performance [14]; TiO$_2$ hollow spheres comprising of nanocrystals/crystallites with exposed high-energy crystal facets were fabricated through a fluoride mediated self-transformation or controlled annealing approaches for high-performance photocatalysis [3,15].

However, the above researches were conducted independently under different conditions through various approaches. It is necessary to explore a general synthetic strategy with reasonable mechanism for surface structure engineering of TiO$_2$ hollow particles, which is also of fundamental importance to promote the development of crystal interface/surface engineering. Furthermore, it is noted that previous successes are often realized on TiO$_2$ hollow

---

spheres with two-/three-dimensional (nanosheet/nanocrystal) surface substructures. Few attempts have been made to fabricate non-spherical TiO_2 hollow structures such as polyhedral nanocages, especially, with textured interfaces/surfaces constituted by one-dimensional (1D) nanostructures. It is demonstrated that anisotropic nanocages with non-spherical shape are particularly interesting due to their unique advantages that are difficult to obtain from conventional structures with round shape [20–23]. Meanwhile, 1D structures have been well known for their unique characteristics of high specific surface [24,25] and high electron mobility [9,10] that are attractive for solar cells [9,10,26], gas sensors [27] and photocatalysis [28–30] as well. Therefore, the effort to construct TiO_2 polyhedral nanocages comprising of 1D nanostructure is highly desired.

In this work we propose to fabricate novel spinous TiO_2-based octahedral nanocages by employing a well-designed synthetic strategy, which involves crystallinity-controlled wet coating of TiO_2 on Cu_2O crystal templates followed by structural ripening and template treating. TiO_2 coating layer with different crystallinity (amorphous to crystalline) from inner to outer layer can be obtained by the programed temperature control. The crystallinity difference of TiO_2 drives surface structural construction during the ripening process and leads to the growth of nanothorns on TiO_2 nanocages. The spinous TiO_2 octahedral nanocages and spinous Au@TiO_2 octahedral nanocages can be facilely produced via the Cu_2O template removal and transformation approaches, respectively. In addition, they exhibit enhanced photocatalytic performance compared with their counterparts of spinousless nanocages, when evaluated with photocatalysis of RhB photodegradation.

2. Experimental section

2.1. Preparation of Cu₂O octahedrons

Cu_2O octahedrons were prepared according to the method reported previously [31]. Briefly, 10 ml of NaOH (2 M) was added dropwise into a 100 mL mixed solution containing $CuCl_2\cdot2H_2O$ (10 mM), sodium citrate (3.4 mM) and poly-(vinylpyrrolidone) (PVP) (0.034 g/mL, Mw = 40,000). After 30 min stirring, 10 mL of ascorbic acid (0.6 M) was added in drops. Then, the solution was incubated at 60 °C for 3 h, leading to a yellow precipitate. The production was centrifuged, washed with ethanol and kept in oven at 60 °C for use.

2.2. Fabrication of spinous TiO₂ and Au@TiO₂ octahedral nanocages

In the typical procedure, a certain amount of Cu_2O templates were dispersed in 25 mL water, followed by the addition of 0.6 mL of 0.02 M TiF4 under stirring. The mixture was then transferred to a 50 mL Teflon autoclave and heated with a ramping rate of 1 °C min^{-1} from 25 to 180 °C. After 30 min reaction at 180 °C, the autoclave was cooled in an oven at the constant temperature of 50 °C for 2 h, resulting in the product of spinous Cu_2O@TiO_2 composite octahedrons. Subsequently, the product was centrifuged, washed and annealed at 450 °C with N_2 gas for 3 h. For the preparation of spinous TiO_2 nanocages, the Cu_2O core templates of the composites were directly removed in a dilute HCl solution. While for the preparation of spinous Au@TiO_2 nanocages, 15 μL of $HAuCl_4$ (40 mM) was added instead, accompanying with the transformation of Cu_2O templates to Au nanoparticles inside TiO_2 nanocages.

2.3. Photocatalysis evaluation

The as-prepared TiO_2 and Au@TiO_2 nanocages with spinous/spinousless surfaces were dispersed on 1.1 cm × 1.1 cm glass substrates and immersed in 10 mL of 5 mg L^{-1} rhodamine B (RhB) aqueous solution. After 30 min stirring in the dark with full adsorption of RhB on catalysts, the system was irradiated using a 300 W high-pressure mercury lamp. The samples were taken out from the solution every 20 min and analyzed by a UV–vis spectrometer to determine residual RhB in solution. The UV-induced degradation of RhB in the solution was estimated with the optical density change of RhB at 554 nm.

2.4. Hydroxyl radical measurement

0.002 g of the as-prepared TiO_2-based catalysts and P-25 powder was respectively dispersed in 20 mL of 10^{-3} M coumarin COU aqueous solution. Subsequently, the well-dispersed suspensions were transferred to quartz cells (9 cm × 9 cm) and kept static to reach an adsorption-desorption equilibrium. A 350 W Xenon arc lamp (equipped in a solar simulator, Newport Co. USA) with a distance of 25 cm above the quartz cells was used as a light source. PL spectra of produced OH radicals were measured by a LS-55 fluorescence spectrophotometer with the excitation wavelength of 332 nm, the scanning speed of 500 nm/min and the width of excitation slit of 2.5 nm. After every 15 min irradiation of Xenon lamp, the sample solution was filtrated to measure the PL intensity at 456 nm.

2.5. Materials characterization

Morphology was characterized using a scanning electron microscope (SEM, Hitachi S4800, 3 kV) equipped with associated energy-dispersive X-ray spectroscopy (EDX) and high-resolution transmission electron microscopy (HR-TEM, JEM 2011, 200 kV). The crystal structure was determined by X-ray diffraction (XRD) using a D/max2550VB3+/PC X-ray diffractometer with Cu Kα radiation with a 1.5418 Å wavelength. A beam voltage of 40 kV and a 100 mA current beam was used. Photoluminescence (PL) spectra were measured by a LS-55 fluorescence spectrophotometer with the excitation wavelength of 332 nm, the scanning speed of 500 nm/min and the width of excitation slit of 2.5 nm.

3. Results and discussion

Fig. 1 shows the synthetic strategy for spinous TiO_2 and Au@TiO_2 octahedral nanocages via a three-step approach including templated coating, controlled structural ripening, and subsequent template removal or transformation. Briefly, Cu_2O octahedral templates were prepared beforehand, followed by TiO_2 wet coating through controlled hydrolysis of TiO_2 precursor. The coating process conducted at programed variable temperatures leads to heterogeneous crystallization with different crystallinities (from amorphous to crystalline) of TiO_2 shells from inner to outer layers. The cystallinity difference causes spontaneous phase transition of TiO_2 from amorphous to crystalline and simultaneous structural construction on TiO_2 shells during ripening process, leading to the formation of TiO_2 nanothorn arrays on Cu_2O@TiO_2 octahedrons, i.e. spinous Cu_2O@TiO_2 octahedrons. Finally, the spinous TiO_2 or Au@TiO_2 octahedral nanocages are formed after respectively removing or transforming Cu_2O octahedrons to Au nanoparticles by the addition of $HAuCl_4$.

SEM images of the typical spinous TiO_2 octahedral nanocages are shown in Fig. 2. It can be seen that the TiO_2 nanocages have a regular octahedral shape with a uniform size (edge length) of about 500 nm (Fig. 2A). Some broken octahedrons show obvious cavities, implying the hollow structure of the TiO_2 nanocages. An enlarged picture displays clearly that there are dense nanothorns growing on the surfaces of the TiO_2 octahedral nanocages. These
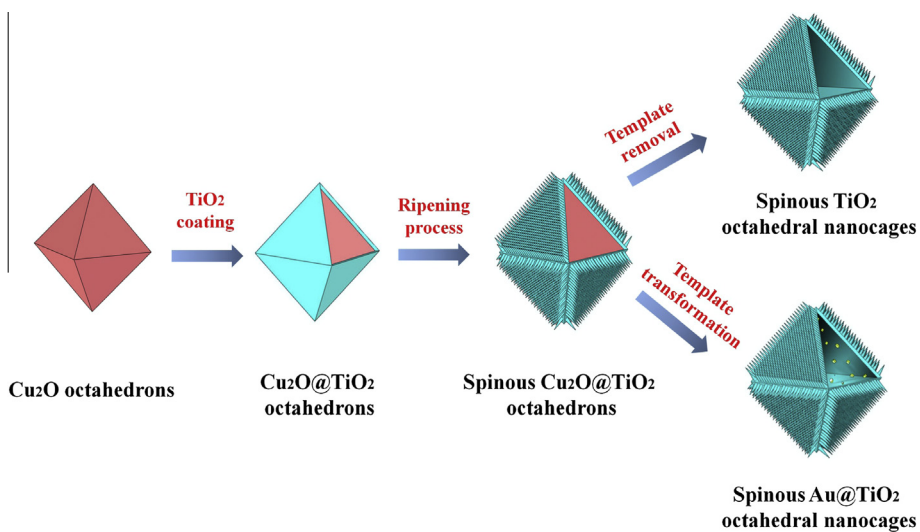
Fig. 1. Schematic illustration for the fabrication of spinous TiO$_2$ and Au@TiO$_2$ octahedral nanocages through a designed strategy involving templated coating, controlled ripening and template removal/transformation.
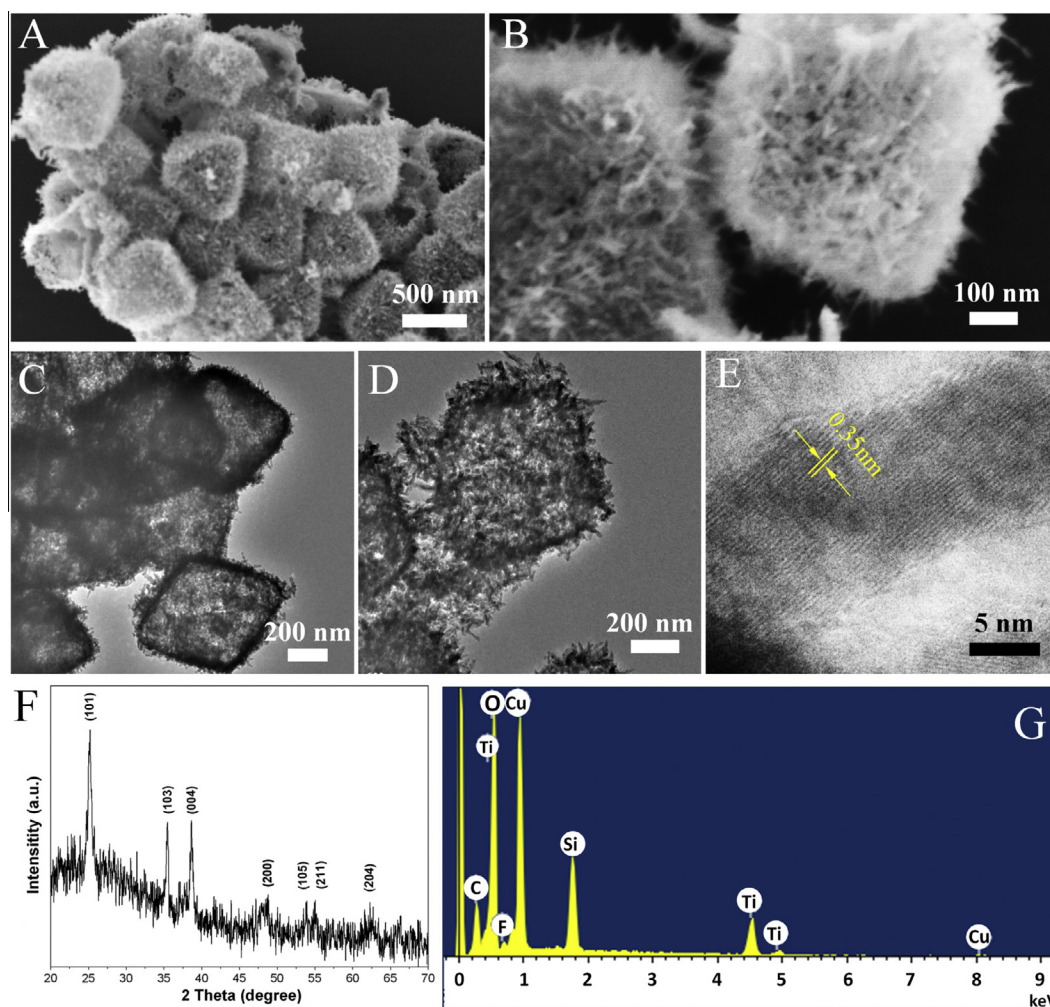

Fig. 2. SEM images (A, B), TEM images (C, D), XRD pattern (E) and EDX panel of spinous TiO$_2$ octahedral nanocages fabricated at programed variable temperatures from 25 to 180 °C.

nanothorns are estimated to be 10 nm in diameter and 50–80 nm in length. Obviously, the size of the spinous TiO_2 nanocages is much larger than that of the Cu_2O octahedron templates (∼250 nm, see Fig. S1), due to the extra thickness of the TiO_2 shell and nanothorns. TEM images of the spinous TiO_2 nanocages are shown in Fig. 2C and D, where the product exhibits a unique structural characteristic that is consistent with the result observed by SEM, such as octahedral shape, hollow interior, thin shell (∼30 nm) and spinous surface. Furthermore, a high-magnification TEM image of an individual nanothorn displays clear crystal lattice fringes with d-spacing of 0.35 nm, corresponding to {1 0 1} planes of anatase TiO_2 (JCPDS card no. 21-1272), indicating that the nanothorn is a single crystal. The XRD pattern (Fig. 2F) of the TiO_2 octahedral nanocages shows several diffraction peaks corresponding well to the anatase TiO_2. Moreover, the Ti and O elements of the

TiO_2 nanocages are also confirmed by the corresponding EDX analysis (Fig. 2G), in addition to C and F elements originated from the chemical agents of PVP and TiF_4, Cu from the Cu_2O templates and Si from the substrate used for SEM measurement.

It is noteworthy that metal/semiconductor nanocomposites have emerged as an important material because of their combined novel optical, electric and catalytic properties with great potential in applications [32–35]. Since Cu_2O can be facilely oxidized by Au^{3+} ions to form metallic Au and soluble Cu^{2+}, the spinous $Au@TiO_2$ octahedral nanocages, a metal/semiconductor nanocomposite, were further prepared by introducing $HAuCl_4$ to the synthetic system, as described in the experimental section. The as-synthesized Au/TiO_2 composite nanocages show a similar spinous morphology, but a different quasi-spherical shape, compared with the spinous TiO_2 octahedral nanocages. It is found that the nanothorns on the
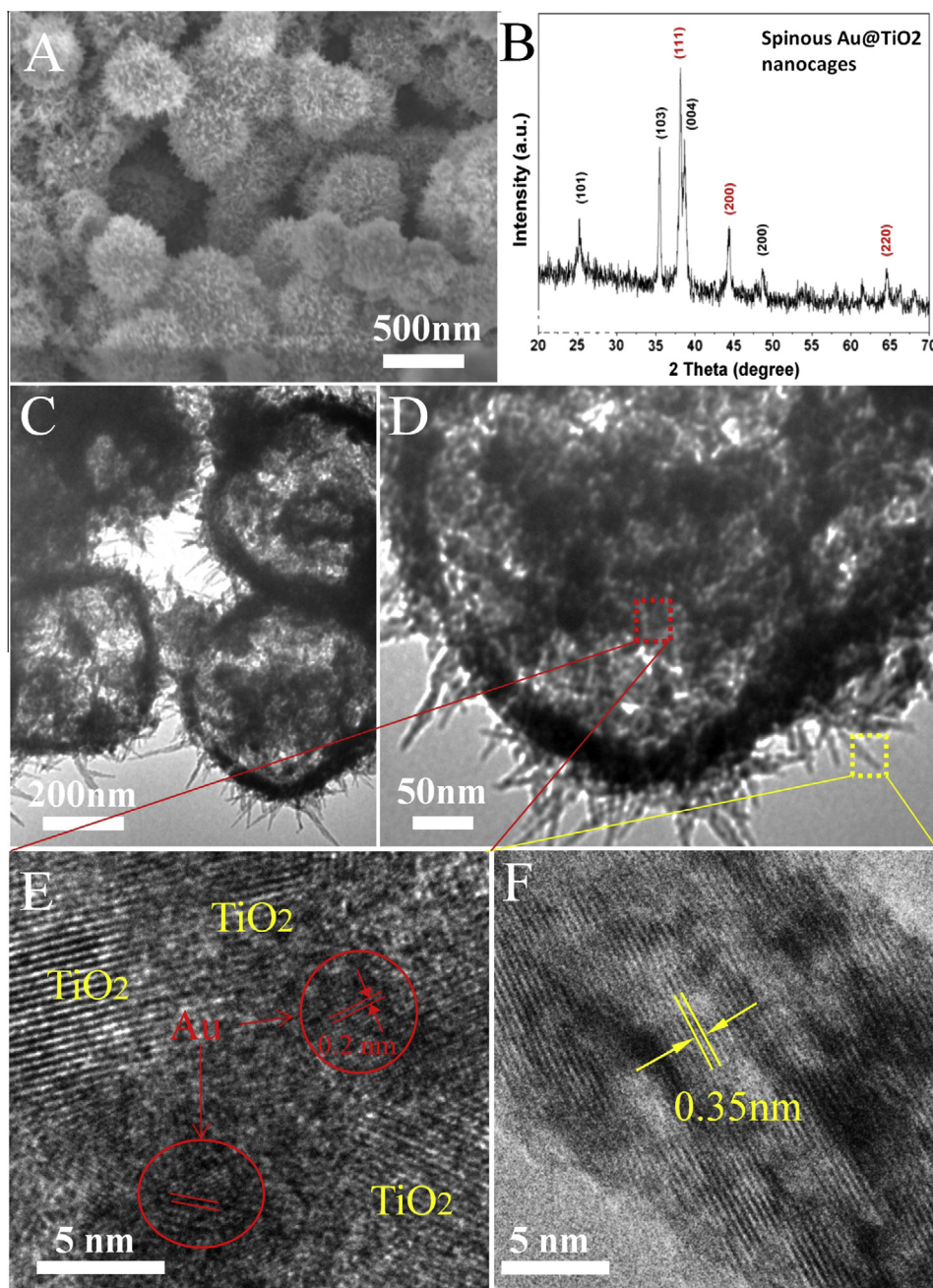

Fig. 3. SEM image (A), XRD pattern (B) and TEM images (C–F) of $Au@TiO_2$ octahedral nanocages at programed variable temperatures from 25 to 180 °C.

Au/TiO$_2$ shells are in a denser and longer manner, due possibly to their further growth under strong acidic conduction of HAuCl$_4$ during the Cu$_2$O core etching process, which leads to the quasi-spherical shape of the composite nanocages in appearance. XRD pattern in Fig. 3B evidences the coexistence of the metallic Au (JCPDS card no.04-0784) and anatase TiO$_2$ (JCPDS card no.21-1272) in the composite octahedral nanocages. The Au@TiO$_2$ composites have hollow structure, thin shells (~30 nm) and spinous surfaces as well, observed from the corresponding TEM images (Fig. 3C and D). High-resolution TEM images give more composition and structural information. As shown in Fig. 3E, a small area in the inner shell of a Au@TiO$_2$ nanocage, corresponding to the red square of Fig. 3D, was selected for closer observation. Some crystallites displaying regular lattice lines with an average d-spacing of 0.2 nm corresponds well to {2 0 0} planes of cubic structured Au, indicating the existence of Au nanoparticles on inner shell of the TiO$_2$ nanocages. In addition, the nanothorns were found to have the same crystal epitaxial structure as that of the spinous TiO$_2$ nanocages (Fig. 3F). These results demonstrate the successful chemical transformation from Cu$_2$O core templates to Au nanoparticles within the TiO$_2$ nanocages and the formation of the novel spinous Au@TiO$_2$ octahedral nanocages.

To investigate the mechanism for the formation of the spinous TiO$_2$-based octahedral nanocages, the effect of key experimental factor such as TiO$_2$ coating temperature, ripening temperature and ripening time has been studied in depth. It was found that if the coating of TiO$_2$ was conducted at a constant temperature such as 180 °C, only the products with smooth surfaces can be obtained. In other words, no structural change on the pre-formed TiO$_2$ shells has been occurred under the same ripening processes for the preparation of either spinous TiO$_2$ or Au@TiO$_2$ octahedral nanocages, as shown in Fig. 4. The coating at constant high temperature will certainly lead to the homogenous crystallization of TiO$_2$ shell. This reveals that the crystallinity difference of TiO$_2$ within the coating
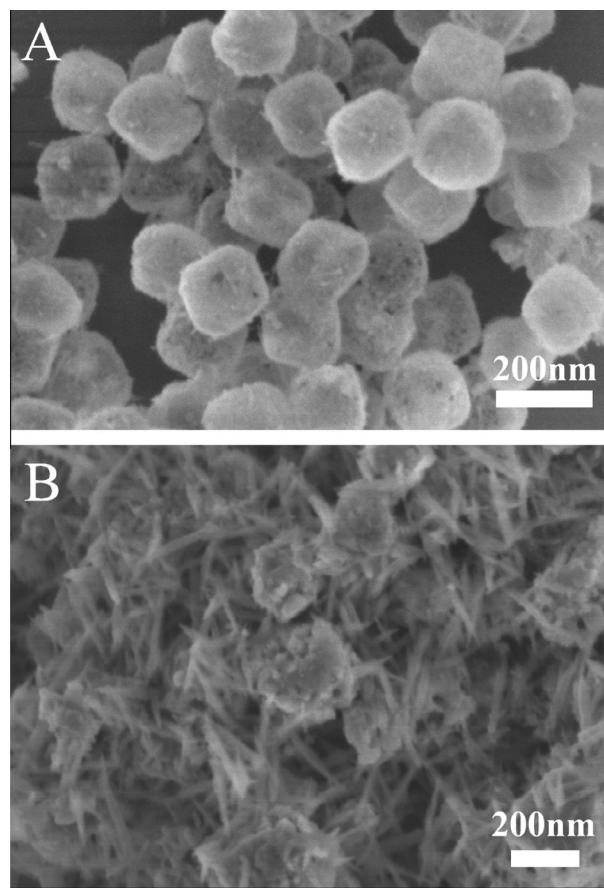

Fig. 5. Ripening time influence on the structure and morphology of TiO$_2$ octahedral nanocages at the typical ripening temperature of 50 °C. (A) 1 h and (B) 4 h.
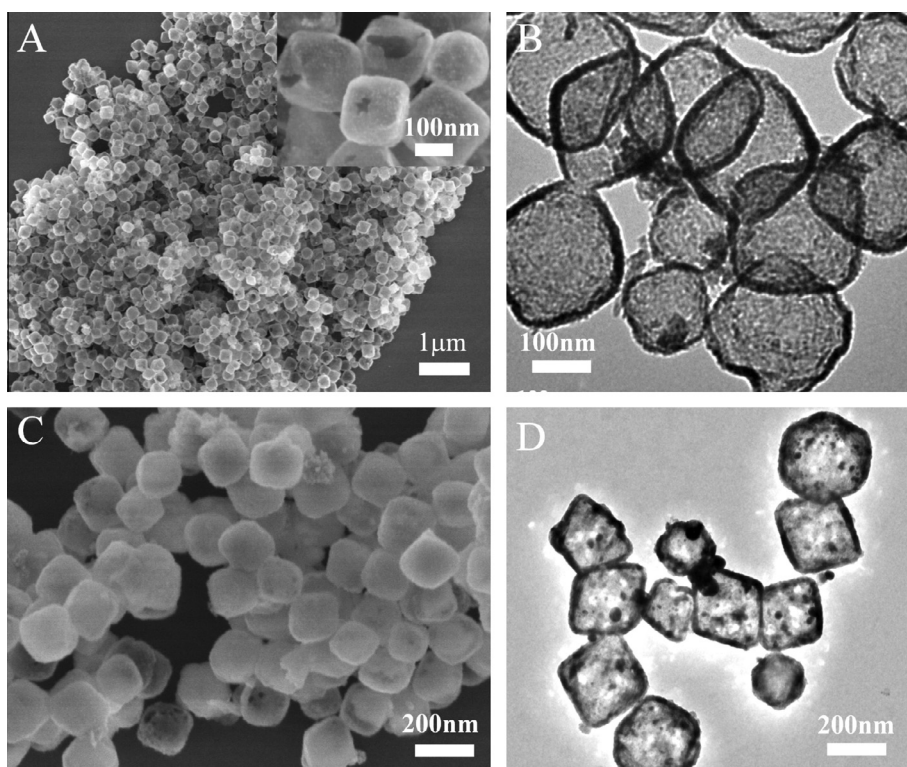

Fig. 4. SEM images of TiO$_2$ and Au@TiO$_2$ octahedral nanocages fabricated at the constant coating temperature of 180 °C.

layer is the driving force for surface structural construction of the TiO$_2$-based nanocages during ripening. Meanwhile, ripening time also has significant influence on the final structure and morphology of the spinous TiO$_2$ nanocages (Fig. 5). With a short ripening time of 1 h, TiO$_2$ octahedral nanocages with sparse and short nanothorns growing on the surface were obtained (Fig. A). In contrast, the size of these TiO$_2$ nanocages is much smaller than the typical spinous TiO$_2$ octahedral nanocages with the ripening time of 2 h, due to the shorter length of nanothorns which is estimated to be less than 10 nm. If increasing the ripening time to 4 h, the TiO$_2$ nanocages were totally broken into pieces, accompanying with overgrown nanothorns (∼30 nm in diameter and ∼200 nm in length) mixed together. Moreover, the contrast experiments at different ripening temperature were also carried out and the results seemed to suggest a similar structure evolution trend. As shown in Fig. 6A, when the ripening was conducted at lower temperature of 25 °C, spinous TiO$_2$ octahedral nanocages with sparsely grown nanothorns were produced. The nanothorns possess a mean
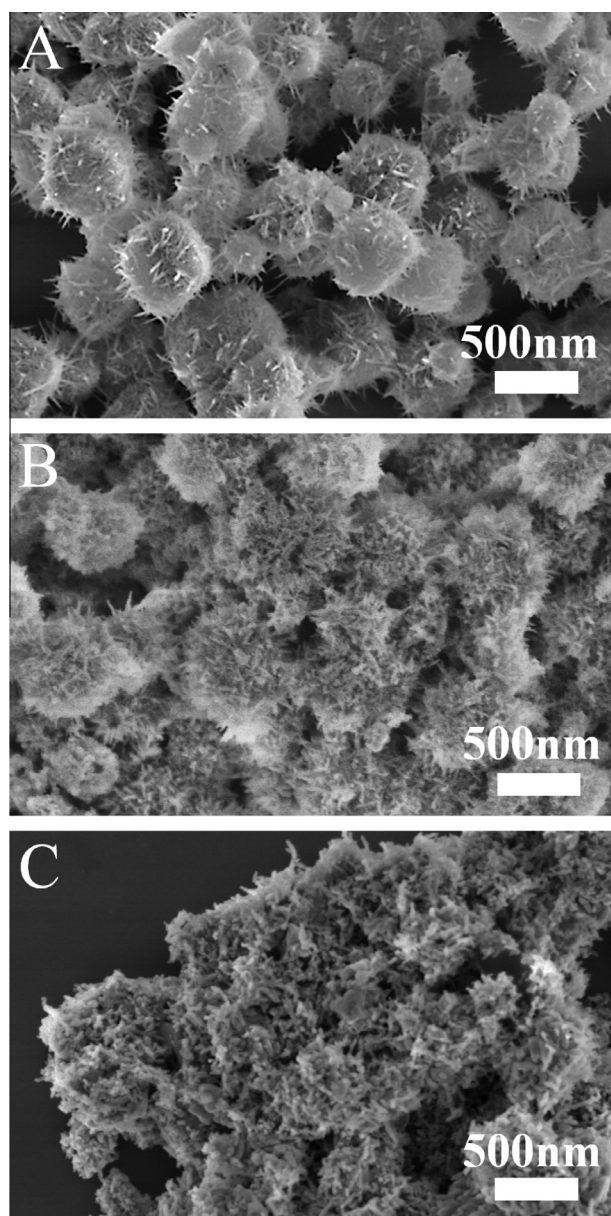
diameter of ∼10 nm and short length of ∼30 nm. If the ripening temperature was moderately elevated to 50 °C, the length (80 nm) and density of nanothorns were increased, forming the typical spinous TiO$_2$ nanocages, as described above in Fig. 2. However, when higher temperatures such as 80 °C or even 180 °C were employed, only partly or totally broken TiO$_2$ nanocages were obtained respectively, in addition to a number of disordered long nanothorns.

Based on the presented results, a plausible proposition for tentatively elucidating the formation mechanism of the spinous TiO$_2$-based nanocages can be given, which emphasizes the critical steps of crystallization-controlled TiO$_2$ coating and subsequent structural ripening driven by amorphisity-to-crystallinity transition. Fig. 7 illustrates the proposed routes for the fabrication of TiO$_2$-based nanocages at different coating temperatures. As generally admitted, the crystallinity of TiO$_2$ depends highly on crystallization temperature. Usually, low-temperature hydrolysis of Ti precursor will lead to the formation of amorphous (for example, at room-temperature, RT) or poor-crystallized TiO$_2$, while temperature elevating can improve TiO$_2$ crystallinity. As shown in Route I, when the TiO$_2$ coating was performed at variable temperatures, i.e., from room temperature of 25–180 °C following the heating program with a ramping rate of 1 °C min^{-1}, TiO$_2$ with different crystallinity (from amorphous to crystalline) changing gradually from inner layer to outer layer of TiO$_2$ shell can be formed. This is supported by the XRD results of three TiO$_2$ nanocages fabricated at different coating temperatures of 90 °C and 180 °C as well as varied temperature of RT-180 °C, where the samples obtained at higher crystallization temperature give higher crystallinity (Fig. S2). On the other hand, according to the well-known "Ostwald ripening" principle, driven by energy minimization, smaller crystallites in aqueous solution can dissolve, diffuse and recrystallize around bigger crystal particles and thereby realize structure reconstruction [36,37]. In our case, an analogous structural construction process driven by amorphisity-crystallinity transition is thought to occur. In general, amorphous TiO$_2$ is more unstable in energy than crystalline TiO$_2$. Therefore, driven by energy minimization, amorphous TiO$_2$ in inner shell is able to "diffuse" to the solution and "re-deposit" on the relatively well-crystallized outer coating layer, namely, the surface of TiO$_2$ nanocages. The continuous dynamic diffusion and redeposition at formed crystal nuclei on the TiO$_2$ nanocages lead to the formation of nanothorns and the spinous TiO$_2$ octahedral nanocages. It is easy to understand that insufficient diffusion and re-deposition will lead to undergrowth of nanothorns and spinous
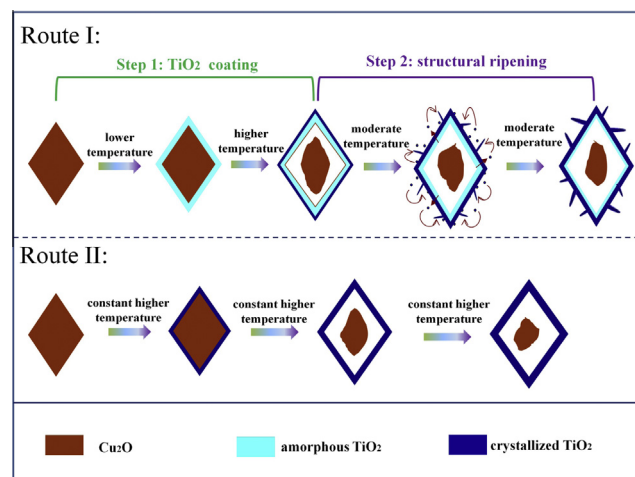

Fig. 6. Ripening temperature influence on the structure and morphology of TiO$_2$ octahedral nanocages with 2 h growth time. (A) 25 °C; (B) 80 °C; (C) 180 °C.

Fig. 7. Schematic illustrating the speculated mechanism for the formation spinous TiO$_2$-based octahedral nanocages.
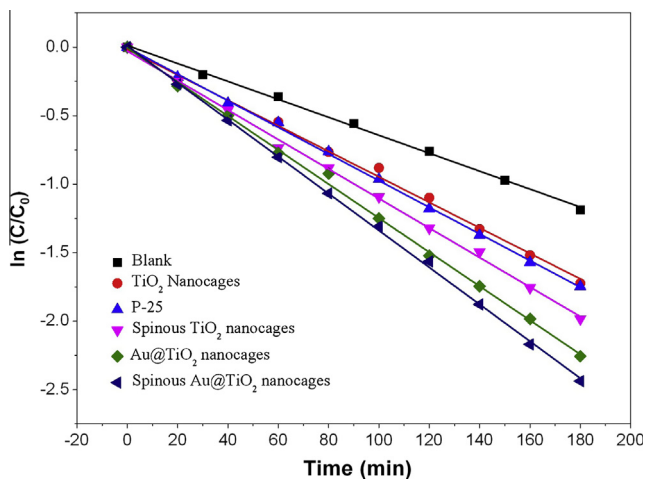
Fig. 8. The photocatalytic properties of the as-prepared TiO₂-based octahedral nanocages as well as P-25 and the blank.

TiO₂ nanocages with sparse and short nanothorns (Figs. 5A and 6A). However, since the growth of nanothorns is at expense of TiO₂ shells, excessively diffusing of TiO₂ from inner shells will result in the collapse of TiO₂ nanocages, simultaneously accompanying with the overgrowth of nanothorns, as shown in the cases of Figs. 5B and 6C and D. In contrast, the coating of TiO₂ conducted at a constant high temperature gives a homogeneous crystallization and a uniform crystallinity throughout TiO₂ shells (Route II), which is much stable in the ripening process and leads to the TiO₂-based nanocages with smooth surfaces (Fig. 4).

The photocatalytic properties of the prepared TiO₂-based octahedral nanocages, as well as commercial Degussa P-25 (P-25) and blank (without photocatalyst added) were evaluated through RhB photodegradation under irradiation of a Hg lamp (300 W). In the measurements, all the samples are deposited on glass substrates with a very small amount mass of about 2.0 mg and normalized to the same area (1.1 cm × 1.1 cm). The results of photocatalytic evaluation for these samples are demonstrated in Fig. 8, which are obtained on the basis of the UV–vis absorption spectra of RhB solution recorded at different degradation times with the TiO₂-based octahedral nanocages as the catalysts (Fig. S3). In principle, the degradation process approximately complies with the pseudo-first-order kinetics

$$\ln\left(\frac{C}{C_0}\right) = -kt \tag{1}$$

where C_0, C and k are the initial concentration of RhB, the real concentrations of RhB corresponding to the exposure time t and the degradation constant, respectively. k values gained from fitted degradation lines for different catalysts of the spinous and spinousless Au@TiO₂ nanocages, the spinous TiO₂ nanocages, P-25, the spinousless TiO₂ nanocages, and the blank are calculated to be 0.01347, 0.01242, 0.01076, 0.00942, 0.00936 and 0.00655 min⁻¹, respectively. There seemed not to have significant differences of magnitude for the k values between the TiO₂-based catalysts and the blank, due probably to the very small amount of the catalysts (mg level) used in RhB photocatalytic degradation. From the calculations, some conclusions with discussion can be given below: (i) the spinous TiO₂-based octahedral nanocages exhibit better photocatalytic performance than spinousless counterparts and P-25. As discussed above, 1D TiO₂ nanostructures hold the unique properties
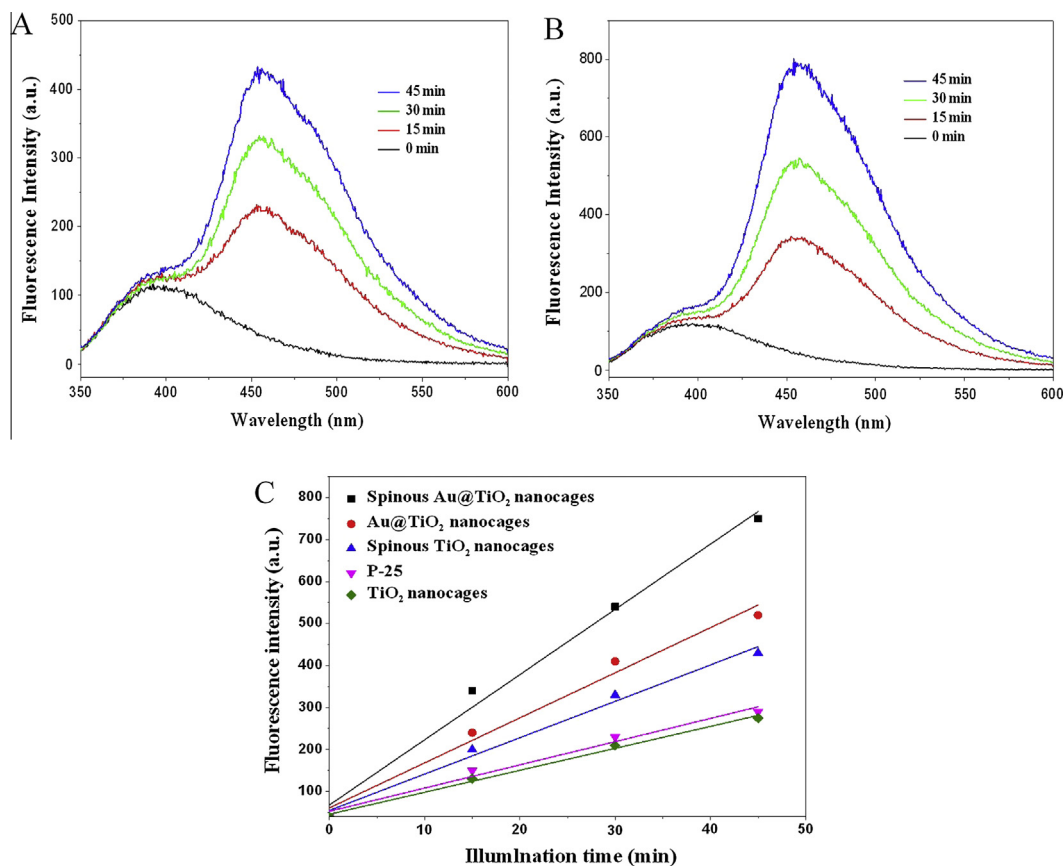

Fig. 9. PL spectral changes observed during illumination ofspinous TiO₂ nanocages (A) and Au@TiO₂ nanocages (B) dispersed in a 10⁻³ M COU aqueous solution, and (C) Plots of concentration of ·OH produced on the TiO₂-based photocatalysts against irradiation time.

of high surface area and high carrier transport [9,10], the growth of 1D nanothorn arrays on the nanocages can endow the catalysts with the capacities of full adsorption for RhB molecules and fast charge transfer along the nanothorns in photocatalysis. Moreover, the spinous nanocages with a dandelion-like morphology may benefit the multiply light reflections between nanocages [18], supposing to obtain higher light harvesting. Therefore, the performance improvements of spinous nanocages are considered to be ascribed to their structure merits which are favorable for high-efficiency photocatalysis. (ii) The Au/TiO$_2$ composite nanocages demonstrate higher photocatalytic activity relative to the pure TiO$_2$ ones including P-25. This should be reasonably attributed to specific effect of the Au–TiO$_2$ heterostructure. It is reported that under UV irradiation, photoelectrons generated from TiO$_2$ will transfer to Au surface through Au-TiO$_2$ interfaces while a quantity of holes are left on the TiO$_2$ surface because of equilibrium band structure of Au and TiO$_2$ [32,33]. As a consequence, photoinduced electrons and holes can be effectively separated and their recombination is significantly suppressed. The effective charge separation will promote the catalytic oxidation/reduction half reactions triggered by active holes and electrons, respectively, and in turn accelerate the overall photocatalytic reactions. In our case, the existence of Au nanoparticles on the inner shell of TiO$_2$ nanocages plays a similar important role in charge separation. It can be envisaged that the well-separated electrons and holes stored in Au nanoparticles and TiO$_2$ nanocage shells may serve as opposite active centers to conduct respective half reactions, for example, O$_2$ reduction and RhB oxidation, accounting for an improved photocatalytic performance.

It is admitted that the formation rate of ·OH radicals on surfaces of irradiated photocatalysts is an active species for direct evaluating the photocatalytic activity of catalysts. The ·OH radicals can be quantitatively detected by the photoluminescence (PL) technique by employing coumarin (COU) as a probe molecule [38,39]. The measurements for various catalysts of the as-prepared TiO$_2$-based nanocages and P-25 were conducted accordingly and the results were shown in Figs. 9 and S4. For all the catalysts, it can be observed that their PL intensities (at 476 nm) are increased monotonically with illumination time (Figs. 9A, B and S4), indicating the concentration of generated OH radicals is proportion to the illumination time. The broad peak around 360–380 nm in the PL spectra corresponds to direct and indirect bandgap transitions of TiO$_2$ materials [40]. In Fig. 9C, the linear relationship between fluorescence intensity and illumination time for the five TiO$_2$-based photocatalysts confirms their good photocatalytic stability. In addition, the formation rate of ·OH radicals for five photocatalysts follows the order below: spinous Au@TiO$_2$ nanocages > Au@TiO$_2$ nanocages > spinous TiO$_2$ nanocages > P-25 ≈ TiO$_2$ nanocages. This order is fully consistent with the order of photocatalytic efficiency of the five catalysts in Fig. 8.

4. Conclusions

In conclusion, spinous TiO$_2$ and Au@TiO$_2$ octahedral nanocages have been fabricated via a three-step strategy involving templated TiO$_2$ coating, subsequent structural ripening and template removal or transformation. A plausible proposition that amorphisity-to-crystallinity transition driven surface structure construction leads to the spinous TiO$_2$-based nanocages have been proposed, on the basis of detailed investigation of key synthetic parameters such as TiO$_2$ coating temperature, ripening time and ripening temperature. In addition, owing to their structure and composition advantages, the synthesized spinous TiO$_2$ and Au@TiO$_2$ octahedral nanocages exhibit enhanced photocatalytic performance in RhB photodegradation, compared with their spinousless counterparts and P-25. The photocatalytic activity of these TiO$_2$ based

photocatalysts was investigated by direct detection of the ·OH radicals generated on surfaces of the irradiated catalysts. When deposited on suitable electrode substrates, the spinous TiO$_2$-based nonspherical nanocages may find great potential as promising electrode materials for solar cells, lithium batteries, and gas sensors. Moreover, our synthetic strategy may be extended as a general method for controlled specific surface/interfacial structure construction for various materials such as metals, hydroxides as well as other oxides.

Acknowledgments

Appendix A. Supplementary material

Supplementary data associated with this article can be found, in the online version, at http://dx.doi.org/10.1016/j.jcis.2014.04.004.

References

[1] H.G. Yang, C.H. Sun, S.Z. Qiao, J. Zou, G. Liu, S.C. Smith, H.M. Cheng, G.Q. Lu, Nature 453 (2008) 638–641.
[2] H.G. Yang, G. Liu, S.Z. Qiao, C.H. Sun, Y.G. Jin, S.C. Smith, J. Zou, H.M. Cheng, G.Q. Lu, J. Am. Chem. Soc. 131 (2009) 4078–4083.
[3] S.W. Liu, J.G. Yu, M. Jaroniec, J. Am. Chem. Soc. 132 (2010) (1916) 11914–11916.
[4] W. Li, Y.H. Deng, Z.X. Wu, X.F. Qian, J.P. Yang, Y. Wang, D. Gu, F. Zhang, B. Tu, D.Y. Zhao, J. Am. Chem. Soc. 133 (2011) 15830–15833.
[5] J.W. Nai, Y. Tian, X. Guan, L. Guo, J. Am. Chem. Soc. 135 (2013) 16082–16091.
[6] A. Fujishima, K. Honda, Nature 238 (1972) 37–38.
[7] R. Asahi, T. Morikawa, T. Ohwaki, K. Aoki, Y. Taga, Science 293 (2001) 269–271.
[8] B. Oregan, M. Grätzel, Nature 353 (1991) 737–740.
[9] B. Liu, E.S. Aydil, J. Am. Chem. Soc. 131 (2009) 3985–3990.
[10] X.J. Feng, K. Shankar, O.K. Varghese, M. Paulose, T.J. Latempa, C.A. Grimes, Nano Lett. 8 (2008) 3781–3786.
[11] X. Chen, S.S. Mao, Chem. Rev. 107 (2007) 2891–2959.
[12] A.L. Linsebigler, G.Q. Lu Jr., J.T. Yates, Chem. Rev. 95 (1995) 735–758.
[13] H.J. Snaith, L. Schmidt-Mende, Adv. Mater. 19 (2007) 3187–3200.
[14] S.J. Ding, J.S. Chen, Z.Y. Wang, Y.L. Cheah, S. Madhavi, X. Hu, X.W. Lou, J. Mater. Chem. 21 (2011) 1677–1680.
[15] Y.Z. Jiao, C.X. Peng, F.F. Guo, Z.H. Bao, J.H. Yang, L. Schmidt-Mende, R. Dunbar, Y. Qin, Z.F. Deng, J. Phys. Chem. C 115 (2011) 6405–6409.
[16] T.J. Zhu, J. Li, Q.S. Wu, Appl. Mater. Interfaces 3 (2011) 3448–3453.
[17] J. Li, Y. Qin, C. Jin, Y. Li, D.L. Shi, L. Schmidt-Mende, L.H. Gan, J.H. Yang, Nanoscale 5 (2013) 5009–5016.
[18] H.X. Li, Z.F. Bian, J. Zhu, D.Q. Zhang, G.H. Li, Y.N. Huo, H. Li, Y.F. Lu, J. Am. Chem. Soc. 129 (2007) 8406–8407.
[19] J.L. Song, H.B. Yang, X. Wang, S.Y. Khoo, C.C. Wong, X.W. Liu, C.M. Li, ACS Appl. Mater. Interfaces 4 (2012) 3712–3717.
[20] M. Hu, J.Y. Chen, Z.Y. Li, L. Au, G.V. Hartland, X.D. Li, M. Marquez, Y.N. Xia, Chem. Soc. Rev. 35 (2006) 1084–1094.
[21] O. Shchepelina, V. Kozlovskaya, S. Singamaneni, E. Kharlampieva, V.V. Tsukruk, J. Mater. Chem. 20 (2010) 6587–6603.
[22] L. Zhang, L. Zhou, H.B. Wu, R. Xu, X.W. Lou, Angew. Chem. Int. Ed. 51 (2012) 7267–7270.
[23] L. Hu, Y. Huang, F. Zhang, Q. Chen, Nanoscale 5 (2013) 4186–4190.
[24] L. Cheng, L.M. Qi, Adv. Mater. 22 (2010) 1494–1497.
[25] L. Schmidt-Mende, J.L. MacManus-Driscoll, Mater. Today 10 (2007) 40–48.
[26] I. Gonzalez-Valls, M. Lira-Cantu, Energy Environ. Sci. 3 (2010) 789–795.
[27] J.H. Yang, G.M. Liu, J. Lu, Y.F. Qiu, S.H. Yang, Appl. Phys. Lett. 90 (2007) 103109.
[28] Z.L. Wang, ACS Nano 2 (2008) 1987–1992.
[29] S.W. Wang, Y. Yu, Y.H. Zuo, C.Z. Li, J.H. Yang, C.H. Lu, Nanoscale 4 (2012) 5895–5901.
[30] Y.H. Zuo, Y. Qin, C. Jin, Y. Li, D.L. Shi, Q.S. Wu, J.H. Yang, Nanoscale 5 (2013) 4388–4394.
[31] Z.Y. Wang, X.W. Lou, Adv. Mater. 24 (2012) 4124–4129.
[32] M. Jakob, H. Levanon, Nano Lett. 3 (2003) 353–358.

[33] V. Subramanian, E.E. Wolf, P.V. Kamat, J. Am. Chem. Soc. 126 (2004) 4943–4950.
[34] D. Buso, J. Pacifico, A. Martucci, P. Mulvaney, Adv. Funct. Mater. 17 (2007) 347–354.
[35] A. Furube, L. Du, K. Hara, R. Katoh, M. Tachiya, J. Am. Chem. Soc. 129 (2007) 14852–14853.

[36] W.Z. Ostwald, Phys. Chem. 34 (1900) 495–503.
[37] H.G. Yang, H.C. Zeng, J. Phys. Chem. B108 (2004) 3492–3495.
[38] Q.J. Xiang, J.G. Yu, W.G. Wang, M. Jaroniec, Chem. Commun. 47 (2011) 6906–6908.
[39] Q.J. Xiang, J.G. Yu, P.K. Wong, J. Colloid Interf. Sci. 357 (2011) 163–167.
[40] S. Nick, L. Darren, F.K. Rafail, J. Phys. Chem. 99 (1995) 16646–16654.